



HAL
open science

A numerical method for cell dynamics: Kinetic equations with discontinuous coefficients

Benjamin Aymard, Frédérique Clément, Frédéric Coquel, Marie Postel

► To cite this version:

Benjamin Aymard, Frédérique Clément, Frédéric Coquel, Marie Postel. A numerical method for cell dynamics: Kinetic equations with discontinuous coefficients. 2012. hal-00751454v1

HAL Id: hal-00751454

<https://hal.science/hal-00751454v1>

Submitted on 13 Nov 2012 (v1), last revised 7 Feb 2013 (v2)

HAL is a multi-disciplinary open access archive for the deposit and dissemination of scientific research documents, whether they are published or not. The documents may come from teaching and research institutions in France or abroad, or from public or private research centers.

L'archive ouverte pluridisciplinaire **HAL**, est destinée au dépôt et à la diffusion de documents scientifiques de niveau recherche, publiés ou non, émanant des établissements d'enseignement et de recherche français ou étrangers, des laboratoires publics ou privés.

A numerical method for cell dynamics: kinetic equations with discontinuous coefficients*

Aymard Benjamin^{†‡}

Clément Frédérique[§]

Coquel Frédéric[¶]

Postel Marie^{†‡}

November 5, 2012

Abstract

The motivation of this work is the numerical treatment of the mitosis in biological models involving cell dynamics. More generally we study hyperbolic PDEs with flux transmission conditions at interfaces between subdomains where coefficients are discontinuous. A dedicated finite volume scheme with a limited high order enhancement is adapted to treat the discontinuities arising at interfaces. The validation of the method is done on 1D and 2D toy problems for which exact solutions are available, allowing us to do a thorough convergence study. A simulation on the original biological model illustrates the full potentialities of the scheme.

keywords: kinetic equations, finite volumes, discontinuous coefficients, cell dynamics

1 Introduction

Our motivation is the numerical simulation of a biological model dedicated to the ovarian follicular development. We adopt the model described in Echenim *et al.* [9] and references therein. This multiscale model describes the latest stages of the follicular development before ovulation. The cell population of each follicle is studied as a density function depending on time, and structured according to two functional space variables, age and maturity. The density functions of the interacting follicles are solutions of weakly coupled PDE-s, where the age and maturity velocities and the loss term depend on the integro-moments of the solution for all the follicles. The moment-based integral formulation accounts in a compact way for the feedback loop involving the ovarian hormones, secreted from follicular cells, and the pituitary hormone FSH (follicle-stimulating hormone) that targets in turn the follicular cells.

*This work is part of the Inria Large Scale Initiative Action REGATE

[†]UPMC Univ Paris 06, UMR 7598, Laboratoire Jacques-Louis Lions, F-75005, Paris, France

[‡]CNRS, UMR 7598, Laboratoire Jacques-Louis Lions, F-75005, Paris, France

[§]Centre de Recherche Inria Paris-Rocquencourt, Domaine de Voluceau, Rocquencourt, B.P. 105 - F-78153 Le Chesnay, France

[¶]CNRS and CMAP, UMR 7641, Ecole Polytechnique, route de Saclay, F-91128 Palaiseau Cedex-France

The model follows the development of the follicles starting from an initial stage where all cells are proliferating. As the granulosa cells progress through subsequent cell cycles their maturity increases up to a threshold beyond which they exit the proliferation cell cycle and enter the differentiation stage D. The control exerted by FSH on cells depends on the cell state, whether the cell be within or outside the division cycle. Moreover, cells become insensitive to any external control during a part of the cycle, leading to a drift dynamics behaving as pure transport.

Cell proliferation is underlain by the process of mitosis, through which a mother cell gives birth to two daughter cells. Mitosis is the endpoint of the cell cycle that consists of the 4 phases G1, S, G2 and M, and ensures proper DNA replication and repartition between the new cells. The most common way of representing mitosis in age-structured models of cell populations is to add a gain term in the right hand side, that controls the (average) doubling time in the cell population (see the renewal equations presented in Chapter 3 of [13]). This is however a rough description of the mitosis event since it is distributed over all cell ages. An alternative way to represent mitosis is to consider appropriate boundary conditions coupling the dynamics of the population of proliferating cells with another population of cells that have exited the cell cycles. Instances of corresponding models can be found in the context of hematopoiesis, the process by which blood cells are produced (see e.g. [1]).

Here, we consider a model where one cannot get rid of discontinuity problems, since not only the mitosis event, but also the distinction between different phases of the cell cycle are embedded in the cell population dynamics. Due to the phase-dependent sensitivity of cells to the extracellular signals that make them progress along the cell cycle, discontinuities on the velocities have to be dealt with in addition to the mitosis-induced discontinuity. More precisely, we account for both the START transition from phase G1 to S and the EXIT transition after mitosis completion [17].

Besides the mitosis process which eventually increases the total cell mass, the follicular development model takes into account apoptosis, and therefore total mass loss, by a source term which is active only locally in a narrow zone delimited by a skewed gaussian law and centered on the boundary between the first phase G1 of the cycle and the differentiation phase. The coefficients of the cell loss term depend on the first moment of the solution.

From the mathematical standpoint the model describes the time evolution of the density function depending on age and maturity variables. This unknown is governed by a kinetic like equation involving velocities that are function of integro-moments of the unknown and the age and maturity variables. Closure equations for these velocities are naturally discontinuous in the age and maturity variables, precisely at biological checkpoints which correspond to the interfaces between the biological phases. These discontinuities require additional information which are handled as local double initial boundary value problems (IBVP), where inner boundary conditions are formulated to express the biological switch [17]. First order equations with discontinuous coefficients have received considerable attention over the past decade. Several existence and uniqueness results have been obtained assuming the conservation of the unknown [6, 8, 14]. In our present setting such conservation property does not hold because of the mitosis process. The well posedness of the resulting PDE model has been successfully studied by Shang [15]. In order to tackle its numerical approximation, various tools are at hand. The general case of transport equations with discontinuous equations was first studied in a series of work by Bouchut and James [4] using duality arguments. Another standpoint is to address those discontinuities in terms of a coupling problem, as pioneered by Godlewski and Raviart [10]. We will adopt this later setting and show that it is well suited to our purpose. We will use techniques proposed in [10] and subsequent studies [2, 5]. Here we pay special attention to the extension of these algorithms to higher order

accuracy, which up to our knowledge, have not yet been addressed.

1.1 Outline

The remaining of the paper is organized in three sections. In Section 2, we describe the problem precisely, and, for sake of simplicity, we reduce it to a linear hyperbolic PDE with piecewise constant speeds and linear source term, in 2D and 1D. In Section 3, we present the numerical scheme. We first recall the Finite Volume scheme and then specifically deal with the transmission conditions. In section 4, we give the results of the numerical validation performed on several 1D and 2D test cases and based on a thorough convergence study. Whenever it is possible, the exact solutions are used as references (the derivation of the analytical solutions is postponed to the appendix). We finally present an instance of implementation of the scheme on the full model of the follicular development.

2 Model

The present work is devoted to the numerical simulation of one single follicle whose density of cell population is denoted by ϕ . This problem is part of the much broader field of coupling problems. Let $\Omega \subset \mathbb{R}^n$, $I \subset \mathbb{R}$, $T > 0$, and $\cup_{i=1}^N \Omega_i = \Omega$ a non overlapping collection of subsets of Ω , a general setup can be mathematically modeled as: find $\phi : [0, T] \times \Omega \rightarrow I$ solution of

$$\begin{aligned} \partial_t \phi + \operatorname{div}(f_i(\mathbf{x}, \phi)) &= S_i(\mathbf{x}, \phi), & \text{on } (0, T) \times \Omega_i, & \quad \forall i = 1 \dots N, \\ \phi(0, \mathbf{x}) &= \phi_0(\mathbf{x}), & \text{on } \Omega, \\ \phi(t, \mathbf{x}) &= 0, & \text{on } (0, T) \times \partial\Omega, \\ \psi_i(\phi(t, \mathbf{x}^-)) &= \phi(t, \mathbf{x}^+) & \text{on } (0, T) \times \Omega_i \cap \Omega_{i+1}, \end{aligned}$$

where $f_i : \Omega_i \times I \rightarrow \mathbb{R}^n$ and $S_i : \Omega_i \times I \rightarrow \mathbb{R}$ are smooth functions. In the last equation modeling the transmission condition between subsets Ω_i and Ω_{i+1} we denote by \mathbf{x}^- (respectively \mathbf{x}^+) the boundary $\Omega_i \cap \Omega_{i+1}$ seen from Ω_i (resp. Ω_{i+1}) side. This setup covers a wide range of applications besides cell proliferation which is our current interest here and which we will detail in the next paragraph: multiphase flow in porous media[5], traffic flow with discontinuous road surface conditions, shape-from-shading problems, sedimentation in thickener-clarifier units [7]., etc, which have generated a lot of interest and mathematical work in recent years.

From the theoretical point of view, one of the specificities of the equation we deal with lies in its quasi linear nature. The flux functions f_i are of the form

$$f_i(\mathbf{x}, \phi) = u(\mathbf{x}, \phi)\phi$$

arising from the weak dependance of the velocity field u on the solution ϕ through its first moments

$$u(\mathbf{x}, \phi) = v(\mathbf{x}, m(t)), \quad \text{with } m_j(t) = \int_{\Omega} x_j \phi(t, \mathbf{x}) d\mathbf{x}.$$

We are furthermore definitely in the non conservative case, since the model exhibits both mitosis – which induces a doubling of the mass – and a locally active source term – inducing a mass loss accounting for the

apoptosis phenomenon. The transmission conditions develop discontinuities in the solution, each time the follicles densities cross half cycle and cycle boundaries or depart in differentiation phase. These discontinuities must be carefully handled, specially with respect to the mass computation which is one of the quantities of interest, along with the maturity.

2.1 2D model of the follicular development

As mentioned in the introduction, in the model proposed in Echenim et al [9] to study the development of ovarian follicles, the cell granulosa density ϕ is a function of time, and two so called space variables, age and maturity. The velocities are differently defined in subregions of the global age-maturity domain as depicted in Figure 1, and can be discontinuous on the interfaces between subregions.

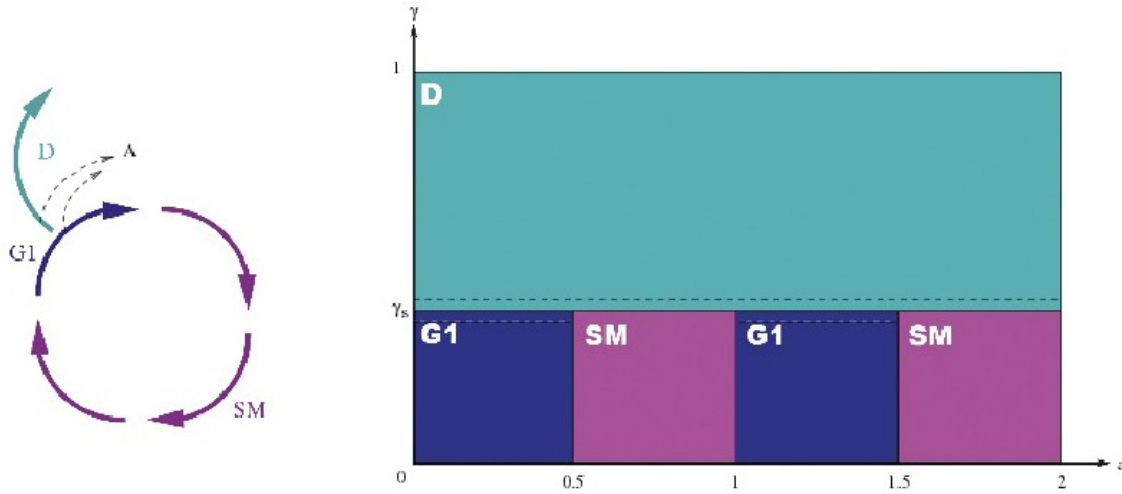


Figure 1: Division of the spatial domain according to the cell phases for unit cycle duration $D_a = 1$. Left : schematic view of a granulosa cell cycle. Right : (a, γ) plane. The bottom part represents the successive cell cycles, each composed of the G1 and SM phases. The top part corresponds to the differentiation phase.

The numerical specificities arising from the coupling between different follicles have been addressed in [3] and we focus here to the case of one single follicle. The density ϕ satisfies the following equation:

$$\frac{\partial \phi(x, y, t)}{\partial t} + \frac{\partial (g(x, y, u(t))\phi(x, y, t))}{\partial x} + \frac{\partial (h(x, y, u(t))\phi(x, y, t))}{\partial y} = -\lambda(x, y, U(t))\phi(x, y, t) \quad (1)$$

set in the computing domain Ω in the (x, y) plane,

$$\Omega = \{(x, y), 0 \leq x \leq N_c \times D_a, 0 \leq y \leq 1\}$$

where N_c is the number of cell cycles and D_a is the duration of one cycle. The domain Ω is divided in zones G1, SM and D, corresponding to different cell states illustrated in Figure 1 and hence different definition of the speeds and source terms. Phase SM in the model aggregates the three latest phases (S, G2, M) of the cell

cycle

$$\begin{cases} \text{G1} = \{(x, y) \in \Omega, & pD_a \leq x \leq (p + 1/2)D_a, & p = 0, \dots, N_c - 1, & 0 \leq y \leq \gamma_s\}, \\ \text{SM} = \{(x, y) \in \Omega, & (p + 1/2)D_a \leq x \leq (p + 1)D_a, & p = 0, \dots, N_c - 1, & 0 \leq y \leq \gamma_s\}, \\ \text{D} = \{(x, y) \in \Omega, & \gamma_s \leq y\}. \end{cases}$$

The aging function g appearing in (1) is defined by

$$g(x, y, u) = \begin{cases} g_1 u + g_2 & \text{for } (x, y) \in \text{G1} \\ 1 & \text{for } (x, y) \in \text{SM} \cup \text{D} \end{cases} \quad (2)$$

where g_1, g_2 are real positive constants. The maturation function h is defined by

$$h(x, y, u) = \begin{cases} \tau_h(-y^2 + (c_1 y + c_2)(1 - \exp(\frac{-u}{\bar{u}}))) & \text{for } (x, y) \in \text{G1} \cup \text{D} \\ 0 & \text{for } (x, y) \in \text{SM} \end{cases} \quad (3)$$

where τ_h, c_1, c_2 and \bar{u} are real positive constants. The source term, that represents cell loss through apoptosis, is defined by

$$\lambda(x, y, U) = \begin{cases} K \exp(-(\frac{(y - \gamma_s)^2}{\bar{\gamma}})) \times (1 - U) & \text{for } (x, y) \in \text{G1} \cup \text{D} \\ 0 & \text{for } (x, y) \in \text{SM} \end{cases} \quad (4)$$

where K, γ_s and $\bar{\gamma}$ are real positive constants.

The equations in the PDE system (1) are linked together through the argument $u(t)$ appearing in the speeds $g(x, y, u)$ and $h(x, y, u)$ and the argument $U(t)$ in the source term $\lambda(x, y, U)$. $U(t)$ and $u(t)$ represent respectively the plasma FSH level and the locally bioavailable FSH level and depend on some maturation moments of the densities. In the case of one single follicle they are identical.

The precise definition of the required transmission conditions has been addressed in the paper by Peipei Shang ([15]). For each cycle $p = 1, \dots, N_c$, the flux on the x -axis is continuous between the zones G1 and SM

$$\phi(t, x^+, y) = (g_1 u + g_2) \phi(t, x^-, \gamma), \quad x = (p - 1/2)D_a, \quad 0 \leq y \leq \gamma_s. \quad (5)$$

The flux is doubling on the interfaces SM-G1, which accounts for the birth of two daughter cells from one mother cell at the end of each cell cycle

$$(g_1 u + g_2) \phi(t, x^+, y) = 2 \phi(t, x^-, y), \quad x = pD_a, \quad 0 \leq y \leq \gamma_s. \quad (6)$$

A homogeneous Dirichlet condition holds to the north of the interface SM-D

$$\phi(t, x, \gamma_s^+) = 0, \quad (p - 1/2)D_a \leq x \leq pD_a. \quad (7)$$

We refer the reader to [3] and the references herein for more details on the model, but nevertheless stress out that, as mentioned in the introduction, an important feature, which is inherent to cell dynamics, is the mitosis event occurring at the interface between zone G and zone SM. In most transport equations dedicated to cell dynamics, it is not accounted for as such but rather by a gain term distributed over the cell population [13]. In [15], the model with discontinuous coefficients was shown to have a unique weak solution, provided that the discontinuities in the velocities were taken into account by flux continuity – at the interfaces between zone G and zone SM – and flux doubling – at the end of each cycle. The SM zone being a transport in age direction only, null flux at the interface with the differentiating zone D ensures the well posedness.

In this paper we will therefore focus on these specific setups, first reducing them to simpler cases where the velocities are given instead of being weakly dependent. The closed-loop case will only be introduced in the final simulation.

2.2 Toy models

For the problem of interest, which is the numerical treatment of the interface conditions (5), (6) and (7), we keep the denominations G1, SM and D stemming out from the biological model for the subregions but simplify the velocities and source coefficient to piecewise constant functions. The weak non linearity arising from the dependence of the speeds and source term on the moments of the solution is left out. It is therefore sufficient to consider a simplified scalar model defined for $(x, y) \in [0, L_x] \times [0, L_y], t > 0$.

$$\begin{cases} \frac{\partial \phi(x, y, t)}{\partial t} + \frac{\partial (g(x, y)\phi(x, y, t))}{\partial x} + \frac{\partial (h(x, y)\phi(x, y, t))}{\partial y} = -\Lambda(x, y)\phi(x, y, t) \\ \phi(x, y, 0) = \phi_0(x, y) & \text{(initial condition)} \\ \psi_L(g(x_s^-, y)\phi(x_s^-, y, t)) = g(x_s^+, y)\phi(x_s^+, y, t) & \text{(flux condition on a vertical edge)} \\ \psi_B(h(x, y_s^-)\phi(x, y_s^-, t)) = h(x, y_s^+)\phi(x, y_s^+, t) & \text{(flux condition on an horizontal edge)} \end{cases} \quad (8)$$

with the piecewise constant velocities $g(x, y)$ and $h(x, y)$ and source term $\Lambda(x, y)$ defined in the subregions depicted on Figure 1. Furthermore, thanks to the simplicity of the geometry, we can use a cartesian grid discretization and a numerical scheme deduced from the 1D problem by tensorization. We will therefore describe the numerical method on the following 1D toy problem

$$\begin{cases} \partial_t \phi(x, t) + \partial_x g(x)\phi(x, t) = -\Lambda(x)\phi(x, t) & \text{for } x \in [0, L_x], t > 0 \\ \phi(x, 0) = \phi_0(x) & \text{(initial condition)} \\ \psi_L(g(x_s^-)\phi(x_s^-, t)) = g(x_s^+)\phi(x_s^+, t) & \text{(flux condition)} \end{cases} \quad (9)$$

with

$$g(x) = \begin{cases} g_L, & \text{for } x < x_s, \\ g_R & \text{elsewhere,} \end{cases} \quad \Lambda(x) = \begin{cases} \Lambda_L, & \text{for } x < x_s, \\ \Lambda_R & \text{elsewhere.} \end{cases} \quad (10)$$

In order to deal with all the situations (5), (6) and (7) encountered in the real-life problem defined by equations (1) to (7), the transmission conditions in (9) will be in turn

$$\psi_L(z) = z \quad \text{(flux continuity between G1 and SM)} \quad (11)$$

$$\psi_L(z) = 2z \quad \text{(mitosis between SM and G1)} \quad (12)$$

$$\psi_L(z) = 0 \quad \text{(waterproof interface between SM and D)} \quad (13)$$

and the source term will be in turn

$$\Lambda_L(x) = \Lambda_R = 0 \quad \text{(No source)} \quad (14)$$

$$\Lambda_L(x) = 1, \Lambda_R = 0 \quad \text{(G1-SM)} \quad (15)$$

$$\Lambda_L(x) = 0, \Lambda_R = 1 \quad \text{(SM-G1)} \quad (16)$$

3 Numerical scheme

We now turn to the numerical method. We first recall the finite volume scheme in the continuous regions, and then present the method that we have designed to deal with the transmission conditions.

3.1 Discretization

In this paragraph we describe the numerical scheme for the simplified problems (9) and (8). We refer the reader to [3] for the discretization of the full biological model (1). To solve (8) we set the domain dimensions as $L_x = L_y = 1$. We denote by N_x the number of grid cells in each direction and by $\Delta x = L_x/N_x$ the space step. The step needs to be chosen so that the locations of the interfaces x_s and y_s , where the speed coefficients $g(x, y)$ and $h(x, y)$ are discontinuous, fall on grid points. From now on we focus on the 1D finite volume scheme to solve (9), since the 2D scheme can be obtained by tensorization. Along the spatial grid

$$x_k = k\Delta x, \quad x_{k+1/2} = (k + 1/2)\Delta x, \quad \text{for } k = 0, \dots, N_x, \quad (17)$$

the time discretization is defined by

$$t^0 = 0, \quad t^{n+1} = t^n + \Delta t^n, \quad \text{for } n = 0, \dots, N_t \quad (18)$$

with N_t such that $t^{N_t} = t_{\text{final}}$, and time steps Δt^n that may change at each iteration, in order to preserve stability. The unknowns are the approximate mean values of the solution in each grid mesh

$$\phi_k^n \approx \frac{1}{\Delta x} \int_{x_k}^{x_{k+1}} \phi(x, t^n) dx. \quad \text{for } k = 0, \dots, N_x - 1.$$

Equation (9) is then explicitly discretized to obtain a recursion formula

$$\phi_k^{n+1} = \phi_k^n - \frac{\Delta t^n}{\Delta x} (F_{k+1}(\phi^n) - F_k(\phi^n)) - \Delta t^n \Lambda(x_{k+1/2}) \phi_k^n \quad (19)$$

where F_k is the numerical flux across x_k , designed using a limiter strategy. Indeed, it is well known that first order schemes, like the Godunov scheme, are diffusive, and that second order schemes, like Lax Wendroff scheme, generate oscillations in the neighborhood of discontinuities. In order to get a stable as well as precise scheme, we take a weighting of a low order scheme and a high order scheme, and we define the limited numerical flux

$$F_k = F_k^{Low} + \ell(r_k)(F_k^{High} - F_k^{Low}), \quad (20)$$

where ℓ is the limiter function designed by Koren [12]

$$\ell_{Koren}(r) = \max(0, \min(2r, \frac{2+r}{3}, 2)),$$

and r_k is defined by

$$r_k = \mathcal{R}((g_{k+i}\phi_{k+i})_{i=-2, \dots, 1}; (g_{k+i})_{i=-2, \dots, 1}) \quad (21)$$

$$\mathcal{R}((z_{k+i})_{i=-2, \dots, 1}; (g_{k+i})_{i=-2, \dots, 1}) = \begin{cases} \frac{z_{k-1} - z_{k-2}}{z_k - z_{k-1}} & \text{if } g_{k+i} \geq 0 \quad \forall i = -2, \dots, 1 \\ \frac{z_{k+1} - z_k}{z_k - z_{k-1}} & \text{if } g_{k+i} \leq 0 \quad \forall i = -2, \dots, 1 \\ 0 & \text{otherwise,} \end{cases} \quad (22)$$

with the notation $g_k = g(x_k)$. This ratio is a good indicator of the regularity of the function (see [16]). In fact, a steep gradient or a discontinuity gives a ratio far from 1, whereas a smooth function gives a ratio close to 1. The first order flux entering equation (20) is the Godunov flux

$$F_k^{Low}(\phi^n) = (g_{k-1}^n)^+ \phi_{k-1}^n + (g_k^n)^- \phi_k^n, \quad (23)$$

and the high order flux is the Lax Wendroff one, which is of second order in space wherever the function $g(x)$ is continuous.

$$F_k^{High}(\phi^n) = \frac{1}{2}(g_{k-1}^n \phi_{k-1}^n + g_k^n \phi_k^n), \quad (24)$$

The CFL stability condition is

$$\Delta t^n \leq \min \left(CFL \frac{\Delta x}{\max_k |g_k|}, \frac{1}{\max_k |\Lambda_{k+\frac{1}{2}}|} \right) \quad (25)$$

with $CFL \leq \frac{1}{2}$ and the notation $\Lambda_{k+1/2} = \Lambda(x_{k+1/2})$.

Choosing Koren limiter in (20) provides third order in space for the convective part of the equation in each domain where it is continuously defined. The source term being discretized by a center point quadrature is at most second order in each domain. Second order in time (third order when $\Lambda = 0$) is achieved by a third order Runge-Kutta method ([11])

$$\begin{aligned} \mathcal{F}_k^1 &= F_{k+1}(\phi^n) - F_k(\phi^n) + \Delta x \Lambda_{k+1/2} \phi_k^n, \\ \phi_k^* &= \phi_k^n - \frac{\Delta t^n}{\Delta x} \mathcal{F}_k^1, \\ \mathcal{F}_k^2 &= F_{k+1}(\phi^*) - F_k(\phi^*) + \Delta x \Lambda_{k+1/2} \phi_k^*, \\ \phi_k^{**} &= \phi_k^n - \frac{1}{4} \frac{\Delta t^n}{\Delta x} \mathcal{F}_k^1 - \frac{1}{4} \frac{\Delta t^n}{\Delta x} \mathcal{F}_k^2, \\ \mathcal{F}_k^3 &= F_{k+1}(\phi^{**}) - F_k(\phi^{**}) + \Delta x \Lambda_{k+1/2} \phi_k^{**}, \\ \phi_k^{n+1} &= \phi_k^n - \frac{1}{6} \frac{\Delta t^n}{\Delta x} \mathcal{F}_k^1 - \frac{1}{6} \frac{\Delta t^n}{\Delta x} \mathcal{F}_k^2 - \frac{2}{3} \frac{\Delta t^n}{\Delta x} \mathcal{F}_k^3, \end{aligned}$$

We will now focus on the interface between two subdomains where the function g can be discontinuous, neglecting the source term for the time being.

3.2 Treatment of discontinuous coefficients

The domain is discretized in such a manner that the interface between two subregions where g is continuous is placed on an edge between two grid cells. Let us consider that the interface position $x_s = x_K$ at the interface between cells $K - 1$ and K as depicted on Figure 2.

To adapt the finite volume scheme designed in the previous paragraph so that it can handle the transmission condition, we define for each interface at grid point x_k two fluxes : the left flux F_k^L and the right flux F_k^R (Figure 2).

Then we rewrite equation (19) as

$$\phi_k^{n+1} = \phi_k^n - \frac{\Delta t^n}{\Delta x} (F_{k+1}^R - F_k^L)$$

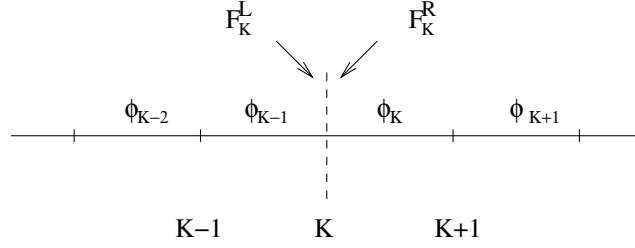


Figure 2: Left and right flux surrounding an interface.

If there is no transmission condition on the flux, we have

$$F_k^L = F_k^R = F_k$$

defined by (20). In contrast, if there is a transmission condition such as (12) for instance, we set

$$F_K^R = \psi_L(F_K^L). \quad (26)$$

The value of the numerical fluxes defined by (23) and (24) are derived for smooth coefficients $g(x)$ and continuous fluxes $g(x)\phi(x)$. They must therefore take into account the transmission condition ψ_L , seen from the left side of x_s . We define, at the interface K , the first order flux

$$F_K^{Low,L}(\phi^n) = (g_{K-1}^n)^+ \phi_{K-1}^n + \frac{1}{2}(1 - \text{sign}(g_K^n))\psi_L^{-1}(g_K^n \phi_K^n), \quad (27)$$

and the second order flux

$$F_K^{High,L}(\phi^n) = \frac{1}{2} (g_{K-1}^n \phi_{K-1}^n + \psi_L^{-1}(g_K^n \phi_K^n)). \quad (28)$$

Furthermore, the high order enhancement using a limited combination such as (20) is affected by the presence of an interface not only at x_K but in its vicinity. Indeed, if the velocity $g(x)$ is positive, the limiter "sees" interface K at neighboring interfaces $k = K - 1, \dots, K + 1$ through the ratio r_k . The transmission condition (26) causes the ratio (21) to depart from 1 on these interfaces and consequently induces a loss of accuracy in the numerical scheme. This can be avoided by computing the ratio r_k on the continuous quantities seen from x_k . Namely, at interfaces $K - 1, K, K + 1$, the limiter is computed using

$$\begin{cases} r_{K-1} = \mathcal{R}(g_{K-3}\phi_{K-3}, g_{K-2}\phi_{K-2}, g_{K-1}\phi_{K-1}, \psi_L^{-1}(g_K\phi_K); (g_{K+i})_{i=-3,\dots,0}) \\ r_K = \mathcal{R}(\psi_L(g_{K-2}\phi_{K-2}), \psi_L(g_{K-1}\phi_{K-1}), g_K\phi_K, g_{K+1}\phi_{K+1}; (g_{K+i})_{i=-2,\dots,1}) \\ r_{K+1} = \mathcal{R}(\psi_L(g_{K-1}\phi_{K-1}), g_K\phi_K, g_{K+1}\phi_{K+1}, g_{K+2}\phi_{K+2}; (g_{K+i})_{i=-1,\dots,2}) \end{cases}$$

instead of (21).

To fix ideas, we apply this method in cases (11) and (12) encountered in our application model.

3.2.1 First application : Flux continuity (with discontinuous speed)

In this case the transmission condition is

$$\psi_L = Id.$$

At interface K , the condition is

$$(g\phi)_K^R = (g\phi)_K^L$$

with

$$g_{K-1} \neq g_K.$$

The transmission condition (26) provides the flux from the right side of the interface

$$F_K^R = F_K^L.$$

The scheme works well without modification, both at first and third order.

3.2.2 Second application : Doubling flux.

In this case the transmission condition (26) is

$$\psi_L(F) = 2F.$$

At interface K , the condition is

$$(g\phi)_K^R = 2(g\phi)_K^L,$$

with

$$g_{K-1} \neq g_K.$$

The flux on the left of the interface is computed using continuous values in the definitions of (23) and (24). From the left side, the continuous values are $g\phi$ for $x < x_K$ and $\psi_L(g\phi)$ for $x > x_K$. Therefore we write for the first order flux

$$F_K^{low,L} = (g_{K-1})^+ \phi_{K-1} + \frac{(g_K)^- \phi_K}{2},$$

and for the second order flux

$$F_K^{high,L} = \frac{g_{K-1} \phi_{K-1} + \frac{g_K \phi_K}{2}}{2}.$$

Concerning the limiter, it has to take the doubling condition on three cells in the vicinity of the interface. At interfaces $K-1, K, K+1$ the limiter (21) is computed on the continuous quantity:

$$\begin{cases} r_{K-1} = \mathcal{R} \left(g_{K-3} \phi_{K-3}, g_{K-2} \phi_{K-2}, g_{K-1} \phi_{K-1}, \frac{g_K \phi_K}{2}; (g_{K+i})_{i=-3, \dots, 0} \right), \\ r_K = \mathcal{R} (2g_{K-2} \phi_{K-2}, 2g_{K-1} \phi_{K-1}, g_K \phi_K, g_{K+1} \phi_{K+1}; (g_{K+i})_{i=-2, \dots, 1}), \\ r_{K+1} = \mathcal{R} (2g_{K-1} \phi_{K-1}, g_K \phi_K, g_{K+1} \phi_{K+1}, g_{K+2} \phi_{K+2}; (g_{K+i})_{i=-1, \dots, 2}). \end{cases}$$

The transmission condition (26) provides the flux from the right side of the interface

$$F_K^R = 2F_K^L.$$

4 Numerical validation

In the sequel, we present several numerical simulations to substantiate the validation of our method. Two 1D situations are handled, one with a flux continuity (11), another one with a doubling at the interface (12), with or without a source term (14), (15), (16). We then present two 2D test cases : a shear phenomenon which is encountered in the realistic model between zones G1 and SM and zones G1 and D, and a waterproof condition (13), which is encountered between zones SM and D. Finally we perform a convergence study on the full biological model.

4.1 1D test cases

For this set of test cases we can compare the numerical solution at final time t_N with the exact solution described in Appendix A.1 and compute the $L1$ -norm relative error

$$E_{\Delta x} = \frac{\sum_{k=0}^{Nx} |\phi_k^N - \bar{\phi}_k^N|}{\sum_{k=0}^{Nx} |\bar{\phi}_k^N|}$$

where $\bar{\phi}_k^N$ is the mean value of the exact solution at final time on cell $[x_k, x_{k+1}]$. This mean value is itself estimated with a quadrature formula – the second order central point formula. This is actually justified for the 1D test cases where the discontinuity of the solution coincides with a grid point. In order to recover the expected behavior the initial condition is a smooth gaussian function of total mass equal to 1 and centered on $x_c=0.3$.

$$\phi_0(x) = \frac{1}{2\pi\sigma} \exp\left(\frac{1}{2} \left(\frac{(x - c_x)^2}{\sigma^2}\right)\right). \quad (29)$$

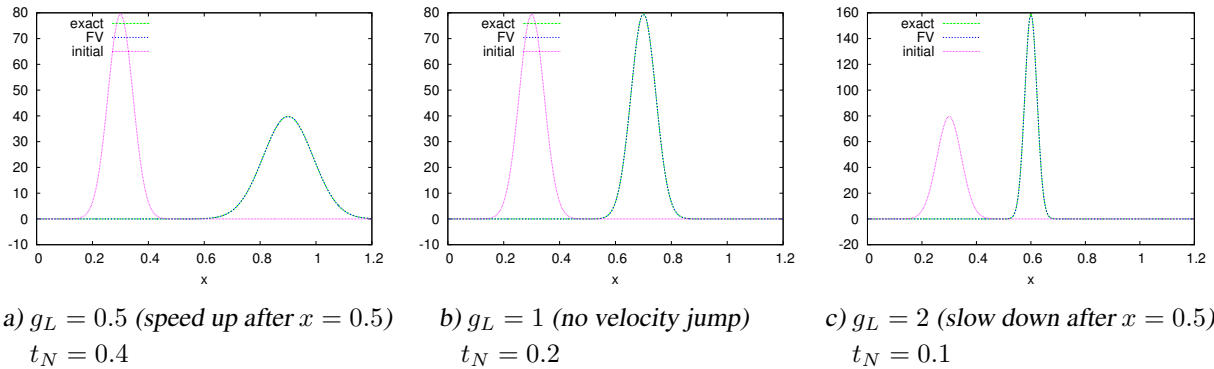


Figure 3: 1D test case 1: flux continuity condition and velocity jump at interface $x = 0.5$. Snapshot of the density $\phi(x, t)$ at initial time and when crossing the interface between zones G1 and SM ($t = t_N$).

test	description	$\psi_L(F)$	g_L	g_R	Λ_L	Λ_R	p	$E \cdot 10^4$
1	Continuous flux, speed discontinuity on G1-SM interface, no source	F	0.5	1	0	0	2.35	9.23
			1				2.39	9.39
			2				2.40	9.74
			3				2.29	9.71
2	Doubling flux, speed discontinuity on SM-G1 interface, no source	$2F$	1	0.5	0	0	2.40	10.25
				1			2.38	9.81
				2			2.35	9.64
				3			2.34	9.61
3	Continuous flux, speed discontinuity on G1-SM interface, source in G1	F	0.5	1	1	0	2.35	8.89
			1				2.39	9.22
			2				2.37	9.47
			3				2.28	9.63
4	Doubling flux, speed discontinuity on SM-G1 interface, source in G1	$2F$	1	0.5	0	1	2.42	10.34
				1			2.36	9.68
				2			2.34	9.60
				3			2.33	9.58

Table 1: 1D test cases description, asymptotic order p of the L1-norm error $O(\Delta x^p)$ and relative error value for $\Delta x = 10^{-3}$. Each test case is run for four different speed contrasts, leading to slightly different asymptotic behaviour.

Test case 1. Continuous flux, speed discontinuity on G1-SM interface, no source

This tests mimics what happens at the transition (11) between zones $G1$ and SM . The speed is equal to 1 in the second half of the domain, and takes values 0.5, 1 (for reference), 2 or 3 in the first half of the domain. As described in Appendix A.1 the exact solution in that case is

$$\phi^{exact}(x, t) = \begin{cases} \phi_0(x - g_L t) & \text{for } x < x_s, \\ g_L \phi_0(x_s - g_L(t - x - x_s)) & \text{for } x_s - t \leq x - t < x_s, \\ \phi_0(x - t) & \text{for } x - t \geq x_s, \end{cases}$$

In Figure 3, we plot the density ϕ at a time $t_N = 0.2/g_L$, chosen so that half the mass has already crossed the interface between zones $G1$ and SM . Since the flux is continuous at $x = 0.5$ and the speed is discontinuous, the solution presents a discontinuity (except for the special case $L_g = 1$). We can notice the good quality of the approximation, compared to the exact solution. There are no oscillations in the neighborhood of the discontinuity, neither numerical diffusion. Remark that if the speed decreases much on the right side of the interface, the density shape sharpens. This is qualitatively similar to what happens for a traffic flow when there is a sudden speed limitation. This phenomenon penalizes the accuracy. In panel b) of Figure 4, the L1-norm error with respect to the space step Δx is displayed in logarithmic scale, which allows us to compute the convergence rate. Depending on the precise value of g_L , the convergence rate varies between 2.26 and 2.4. More precisely, it gets worse as the value of g_L . This can be explained by looking at the contrast between g_L and $g_R = 1$. By analogy with the traffic flow, the interface between a high speed on the left and a lower one on the right hand side corresponds to a sudden speed decrease which generates an accumulation of traffic. The density profile becomes narrower and it becomes harder to make accurate simulations. In contrast, when

the speed is higher on the right, the density profile becomes smoother and it becomes easier to approximate the solution. In any case, the best order of convergence 2.4 is achieved when $g_L = g_R = 1$. In panel a) of Figure 4, the total mass

$$m_0(t) = \int_{[0,L]} \phi(x,t) dx$$

is displayed with respect to the time to check whether the scheme is conservative.

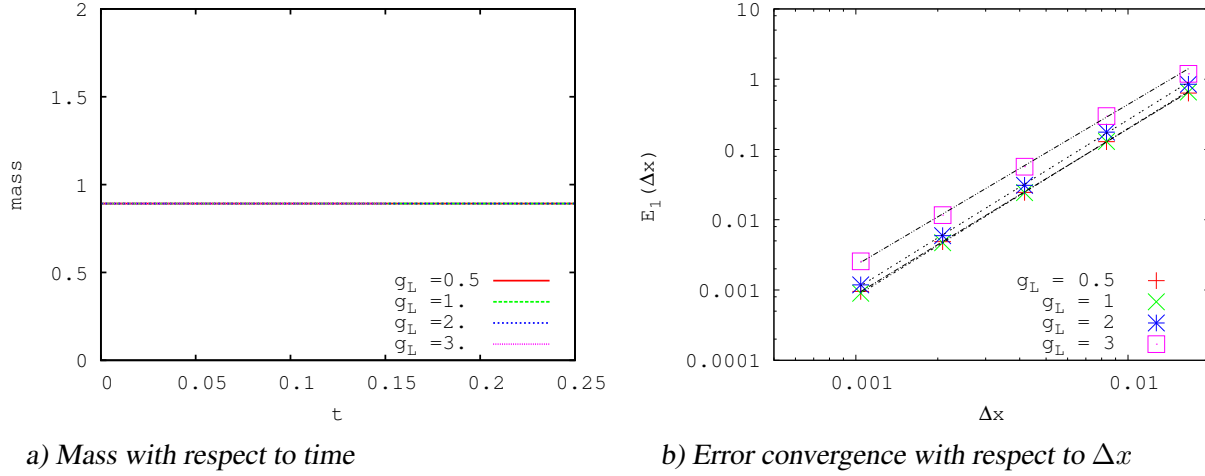


Figure 4: 1D test case 1: flux continuity condition and velocity jump at interface $x = 0.5$. In panel a) the total mass remains constant with time. In panel b) the L_1 -norm error goes to 0 with Δx . The convergence rates (around 2.4) are gathered in Table 4.1.

We also perform a 2D generalization of this test in the case $g_L = 2$, with a smooth initial condition

$$\phi_0(x, y) = \frac{1}{2\pi\sigma^2} \exp\left(\frac{1}{2} \left(\frac{(x - c_x)^2}{\sigma^2} + \frac{(y - c_y)^2}{\sigma^2} \right)\right). \quad (30)$$

centered on $(c_x, c_y) = (0.3, 0.15)$ and the same variance $\sigma^2 = 0.002$ as before. The corresponding results are displayed on Figure 5.

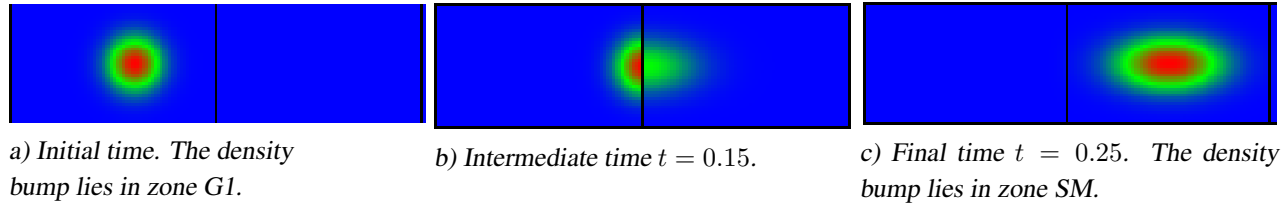


Figure 5: 2D visualization of test case 1: flux continuity condition and velocity jump at interface $x = 0.5$, $u_L = 0.5$, $u_R = 1$. Snapshot of the density (initial time, passing interface, final time). ($CFL = 0.4$, $\Delta x = 0.001$).

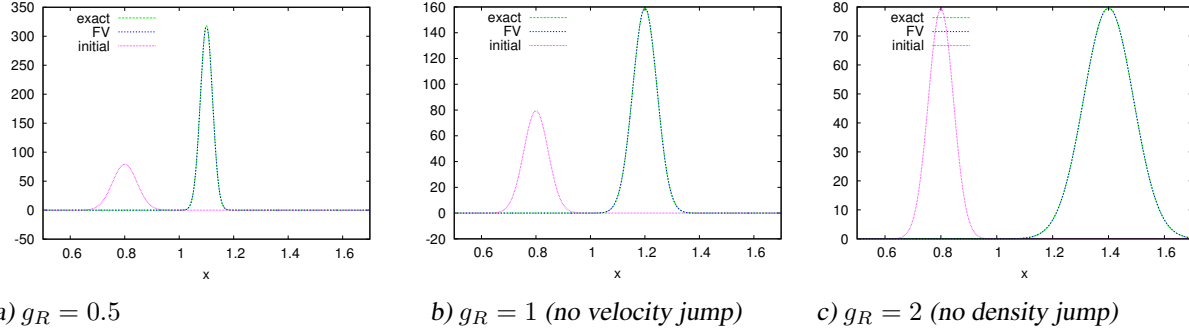


Figure 6: 1D test case 2: doubling flux condition and velocity jump at interface $x = 1$. Snapshot of the density $\phi(x, t)$ at initial time and when crossing the interface between zones G1 and SM ($t = 0.2$).

Test case 2. Doubling flux, speed discontinuity on SM-G1 interface, no source

The second test case mimics the mitosis (12) event occurring between the SM and G1 zone at $x_s = 1$. The spatial range of interest is thus shifted to $[0.5, 1.7]$. The initial condition is centered on $x_c = 0.8$. The speed is equal to $g_L = 1$ for $x < x_s$ and takes successively the values $g_R = 0.5, 1, 2$ or 3 for $x > x_s$. This time the exact solution is

$$\phi^{exact}(x, t) = \begin{cases} \phi_0(x - t) & \text{for } x < x_s, \\ \frac{2}{g_R}(\phi_0(x_s - t - \frac{(x-x_s)}{g_R})) & \text{for } (x_s - g_R t) \leq (x - g_R t) < x_s, \\ \phi_0(x - g_R t) & \text{for } (x - g_R t) \geq x_s, \end{cases}$$

In Figure 6, we plot the density ϕ at time $t = 0.2$. This corresponds to the time at which half the mass has already crossed the interface between zones SM and G1. The solution is continuous when $g_R = 2$, but exhibits a discontinuity in slope. We can draw the same conclusions as the first test case. In particular, there are no oscillations in the neighborhood of the discontinuity, even if there is a discontinuity in the solution.

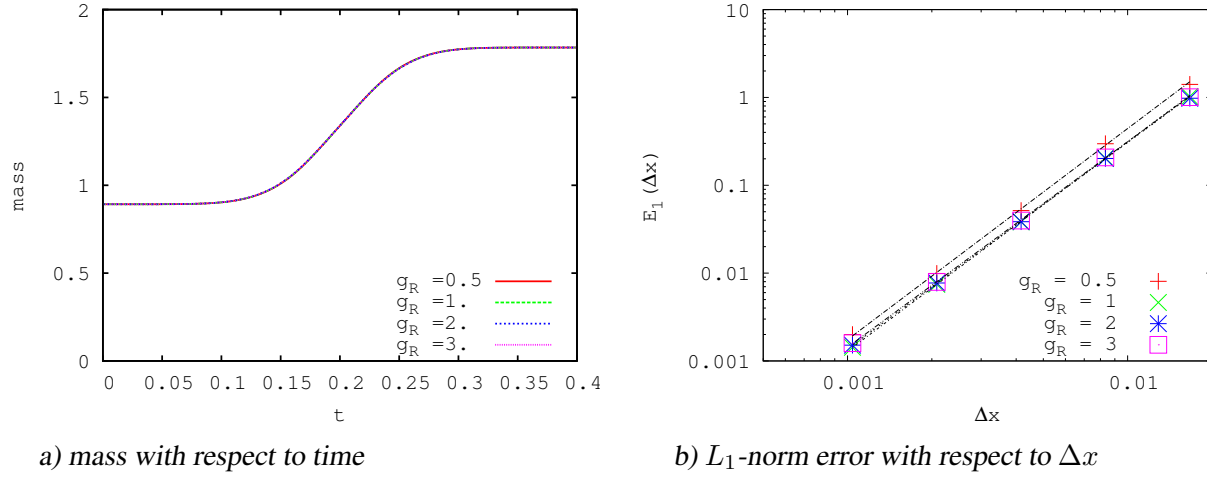


Figure 7: 1D test case 2. Doubling flux condition and velocity jump at interface $x = 1$. The mass in panel a) has doubled when all the density has reached the second subdomain, as expected. In panel b) the L_1 -norm error goes to zero with Δx . The convergence rates (around 2.4) are displayed in Table 4.1.

In panel b) of Figure 7 we plot in a log scale the L_1 -norm error with respect to the space step Δx . The convergence rates, gathered in Table 4.1, are similar to the first test case, which means that the transition condition has not reduced the precision of the scheme. We can notice that the lower the g_R , the worse the error. This is the inverse situation to the first test case which can be explained by the same analogy with the traffic flow. In panel a) of Figure 7 we plot the mass with respect to time. Once all the cells have been transported in the right subdomain, the mass is doubled. As expected, since the speed is always $g_L = 1$ in the left subdomain, in all cases the densities reach the interface at the same time and the mass profiles are identical. Figure 8 displays the 2D generalization of the second test case with the initial condition (30) centered this time on $(c_x, c_y) = (0.8, 0.15)$.

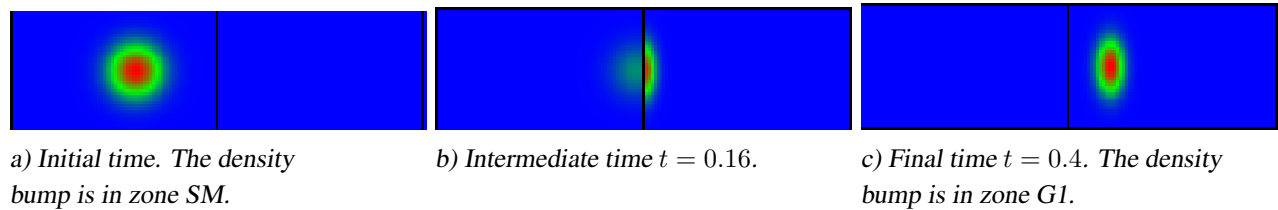


Figure 8: 2D visualization of test case 2. Doubling flux condition and velocity jump at interface $x = 1$ $u_L = 1, u_R = 0.5$. Snapshots of the density (initial time, passing interface, final time). The mass is doubling. ($CFL = 0.4, \Delta x = 0.001$).

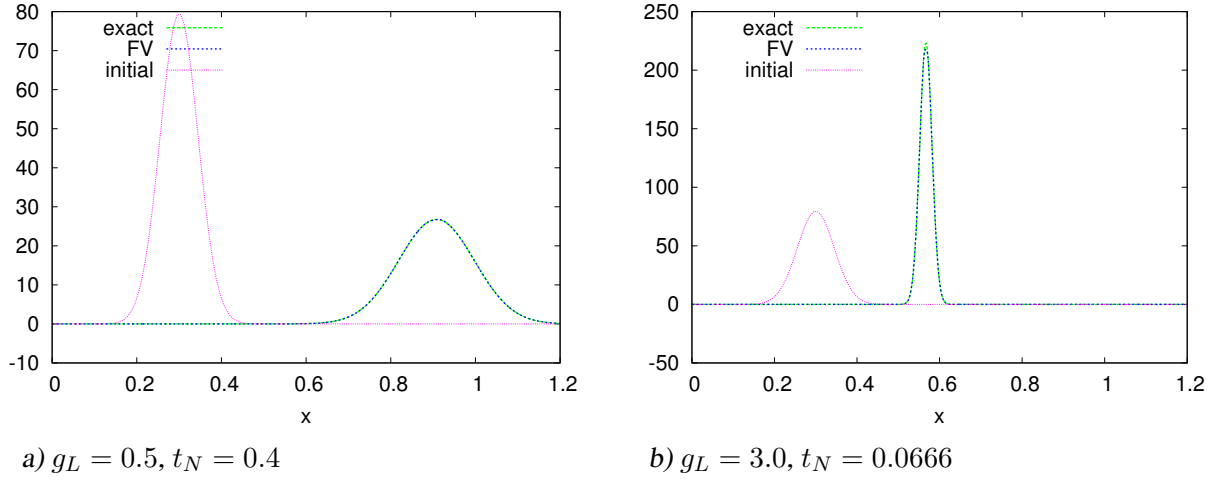


Figure 9: 1D test case 3: flux continuity condition and velocity jump at interface $x = 0.5$, with source on the left. Snapshot of the density at initial time and when crossing the interface between zones G1 and SM ($t = t_N$).

Test case 3. Continuous flux, speed discontinuity on G1-SM interface, linear source on the left

The third test case is the same as the first one but with a linear source term $\Lambda_L = 1$ in the left part of the domain. The exact solution, detailed in Appendix, is

$$\phi^{exact}(x, t) = \begin{cases} \phi_0(x - g_L t) \exp(-t) & \text{for } x < x_s, \\ g_L \phi_0(x_s - g_L(t - x - x_s)) \exp(-t + x - x_s) & \text{for } x_s - t \leq x - t < x_s, \\ \phi_0(x - t) & \text{for } x - t \geq x_s, \end{cases}$$

As in the first test case, we plot the density at time t_N , when half the mass has already crossed the interface between zones G1 and SM. Two cases $g_L = 0.5$ and $g_L = 3$ are represented respectively on panels a) and b) of Figure 9. The convergence study is illustrated in panel b) of Figure 10. The scheme still works well with the source term, although the asymptotic order for the L_1 -norm error is 2.4, which is slightly less accurate than without the source term. Since the source term is active on the left subdomain, there is a loss in mass until the density bump reaches the interface (see panel a) of Figure 10). In the case where $g_L = 3$, the mass stabilizes after the density has passed through the interface. In the case where $g_L = 0.5$ the density bump has not entirely passed through the interface at $t = 0.25$ so that the mass is not yet stabilized. cette remarque est intéressante pour l'application bio: le temps de transit dans la zone où le terme d'apoptose est actif conditionne en partie la masse finale.

Test case 4. Doubling flux, speed discontinuity on SM-G1 interface, linear source

The fourth test case is the same as the second one but with a linear source term $\Lambda_R = 1$ in the right part of the domain. The exact solution is then

$$\phi^{exact}(x, t) = \begin{cases} \phi_0(x - t) & \text{for } x < x_s, \\ \frac{2}{g_R}(\phi_0(x_s - t - \frac{(x-x_s)}{g_R}))e^{\frac{x_s-x}{g_R}} & \text{for } (x_s - g_R t) \leq (x - g_R t) < x_s, \\ \phi_0(x - g_R t)e^{-t} & \text{for } (x - g_R t) \geq x_s, \end{cases}$$

As in the second test case, we plot the density at time $t = 0.2$, for two values $g_R = 0.5$ and $g_R = 3$ respectively on panels a) and b) of Figure 11. Here also the asymptotic order of convergence for the error is roughly 2.4 (see panel b) of Figure 12). The source term is active in the right subdomain. The mass, observed in panel a) of Figure 12, first doubles as the density bump goes through the interface, then diminishes as soon as the loss term becomes active. The drop in mass begins at the same time in both cases $g_R = 0.5$ and $g_R = 3$ since the interface is reached with the same left speed. In the biological model the final mass is indeed the result of the proliferation due to mitosis, compensated by the loss due to apoptosis.

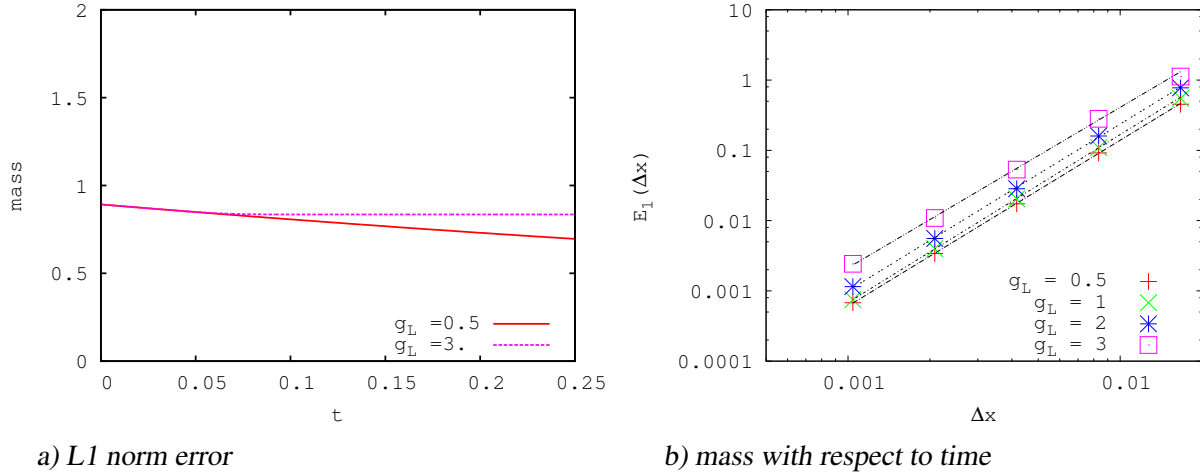


Figure 10: 1D test case 3: flux continuity condition and velocity jump at interface $x = 0.5$, linear source on the left. In panel a) the mass decreases with time before the density has passed the interface ($CFL = 0.4$, $\Delta x = 0.001$). In panel b) the L_1 -norm error goes to zero with Δx . The convergence rates (around 2.4) are displayed in Table 4.1.

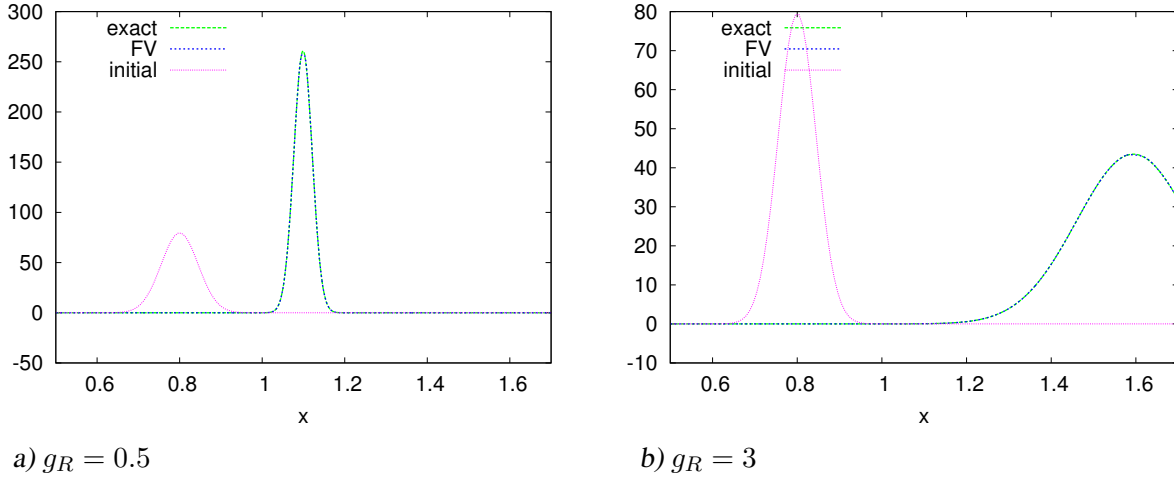


Figure 11: 1D test case 4: doubling flux condition and velocity jump at interface $x = 0.5$, linear source on the right. Snapshot of the density $\phi(x, t)$ at $t = 0$ and $t = 0.2$, crossing the interface between zones SM and G1.

4.2 2D test cases

We now turn to the validation of the method in 2D. As shown on Figure 1, the computing domain includes four internal boundaries: two vertical ones between zones G1 and SM and SM and G1, and two horizontal ones, between zones G1 and D and SM and D. The initial condition is centered on $(c_x, c_y) = (0.3, 0.15)$.

4.2.1 Error Computing

In 2D the relative error due to discretization is computed with

$$E(\Delta x) = \frac{\sum_{k=0}^{Nx-1} \sum_{l=0}^{Ny-1} |\phi_{k,l}^N - \bar{\phi}_{k,l}^N|}{\sum_{k=0}^{Nx-1} \sum_{l=0}^{Ny-1} |\bar{\phi}_{k,l}^N|} \quad (31)$$

where $\bar{\phi}_{k,l}^N$ is the mean value of the exact solution on the grid cell $[x_k, x_{k+1}] \times [y_l, y_{l+1}]$ at time t_N . This value is computed using the 2nd order quadrature formula in the first three test cases where the exact solution is explicitly known. When we do not know the exact solution, we use a reference solution, ϕ^{fine} , computed on a very fine grid with N_x^{fine} cells, and project it on the current grid with N_x^{coarse} cells

$$\bar{\phi}_{k,l}^N = \sum_{i=1}^m \sum_{j=1}^m \phi_{km+i, lm+j}^{fine, N}$$

with

$$m = \frac{N_x^{fine}}{N_x^{coarse}}.$$

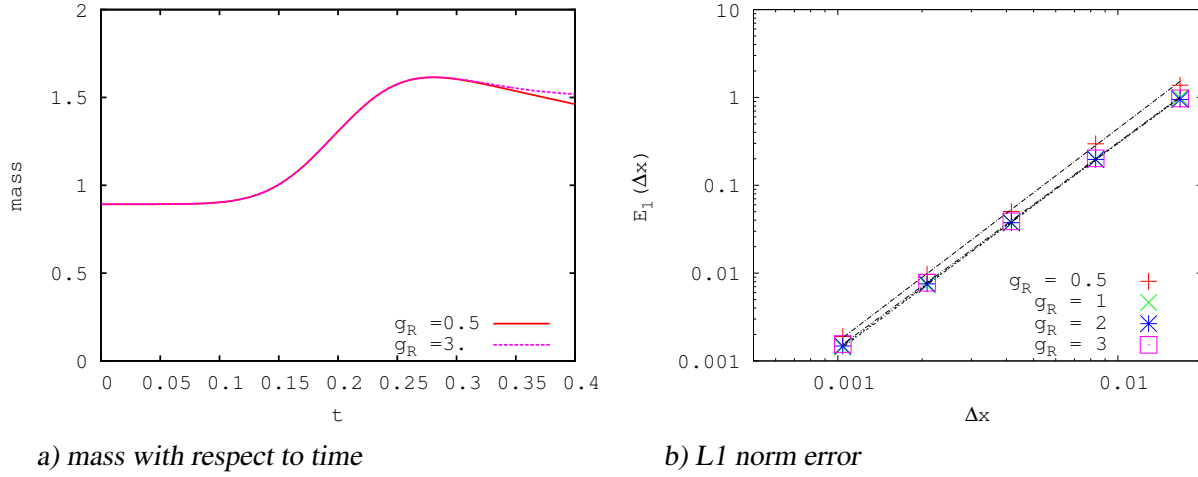


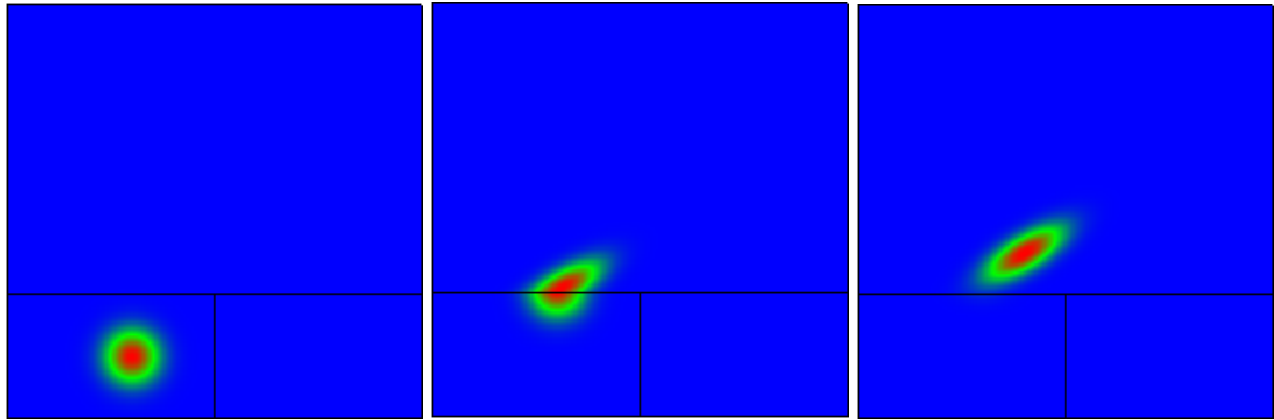
Figure 12: 1D test case 4: doubling flux condition and velocity jump at interface $x = 0.5$, linear source on the right. The mass increases just after the interface, then decreases when the density has passed the interface. The convergence rates (around 2.4) are displayed in Table 4.1.

2D test case 1 : shear interface

For this test case the speed is vertical $g(x, y) = 0$, $h(x, y) = 1$ in the bottom part of the computing domain ($G1 \cup SM$). In the top part (D), the speed is oblique $g(x, y) = 1$ and $h(x, y) = 1$. The discontinuity in speed is located on the x -axis at $y_s = 0.3$. On the snapshots in Figure 13, we can observe a shear phenomenon that could not occur in 1D. We also notice that the change of direction of the speed transforms the shape of the density bump, from circular to elliptic. The total mass remains constant. Due to the shear, the asymptotic rate of convergence of the error drops to 2.1 (see panel a) of Figure 14).

4.2.2 2D test case 2: waterproof interface

In this test case, the speed is diagonal $g(x, y) = 1$, $h(x, y) = 1$ in zone $G1 \cup D$, and horizontal $g(x, y) = 1$, $h(x, y) = 0$ in zone SM . On the snapshots in Figure 15, we can observe a phenomenon of waterproof interface that could not occur in 1D. The fraction of the mass which crosses the vertical interface between zones $G1$ and SM remains trapped in zone SM and can only move horizontally. The convergence rate drops to 1 (panel b) of Figure 14).

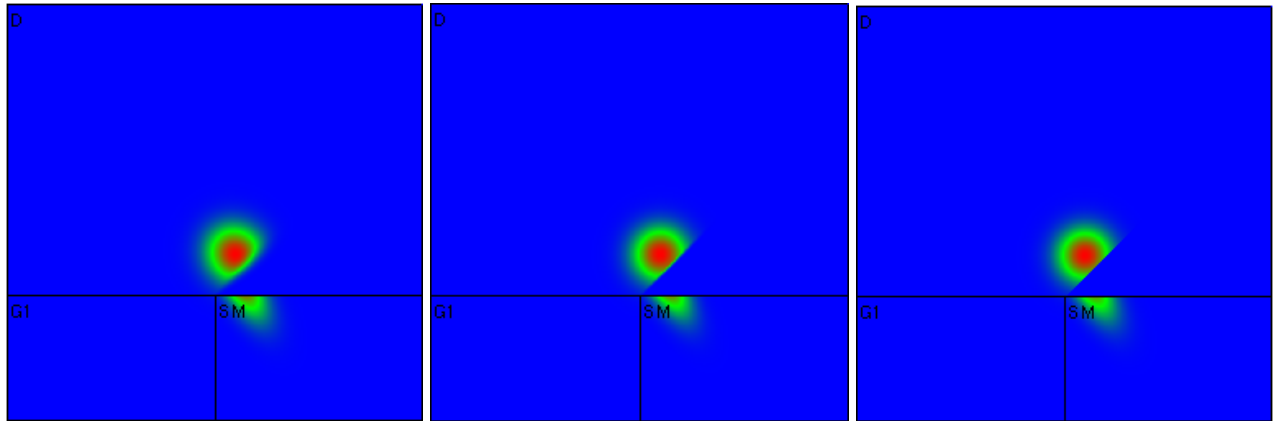


a) Initial time. The density bump lies in zone G1.

b) Intermediate time $t = 0.15$.

c) Final time $t = 0.25$. The density bump lies in zone D.

Figure 13: First 2D test case, shear phenomenon. Snapshot of the density (initial time, passing interface, final time). ($CFL = 0.4, \Delta x = 0.001$).



a) First order approximation.

b) Third order approximation.

c) Exact solution.

Figure 15: 2D test case 2 : waterproof interface. Density at final time (First and third order computations and exact solution). Some numerical diffusion affects the shape of the density, due to the splitting of the initial density bump into two separate clouds.

In order to understand better the drop in precision for the 2D test case 2, we have studied other values for $h(x, y) = h_B$ in the zone SM, ranging from the reference case with no speed variation ($h_B = 1$) and the waterproof test case ($h_B = 0$). Figure 16 displays the density at time $t = 0.25$ for three different h_B values. For $h_B = 0.9$, the solution displayed on panel a) looks very much like that obtained with the reference case. For $h_B = 0.001$, the solution displayed in panel c) looks very much like that obtained with the waterproof boundary in Figure 15.

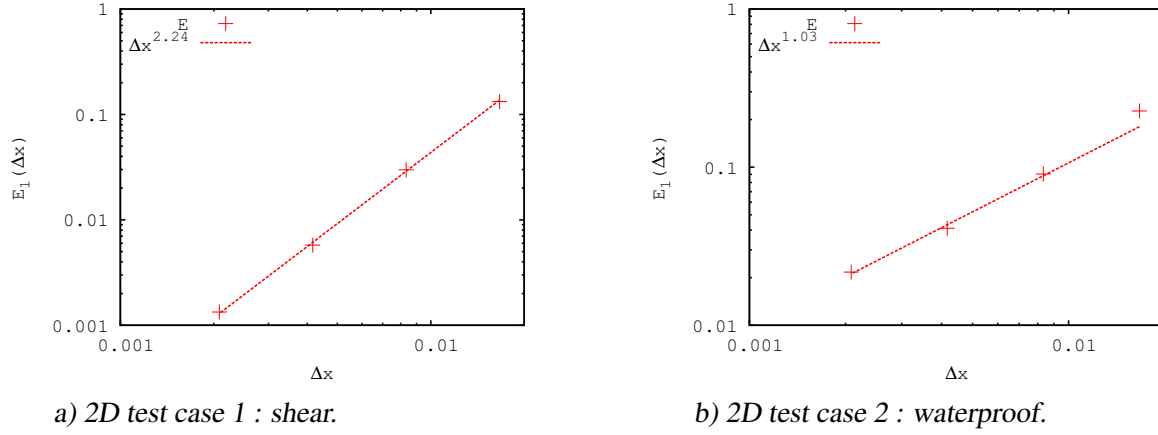


Figure 14: 2D test cases. L_1 -norm relative error with respect to Δx . The convergence rate is 2.24 in the shear case (panel a) and drops to 1.03 in the waterproof case (panel b).

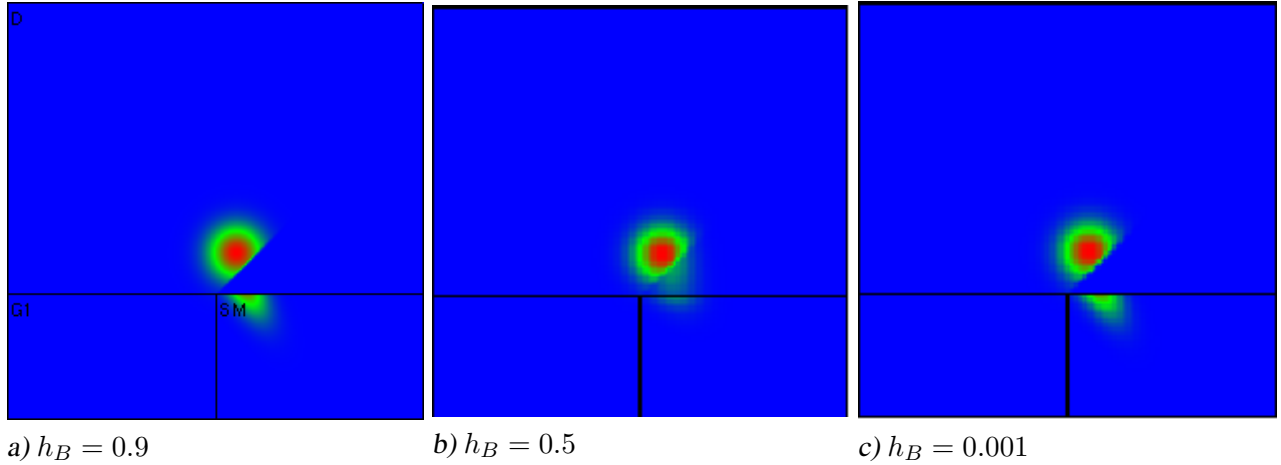
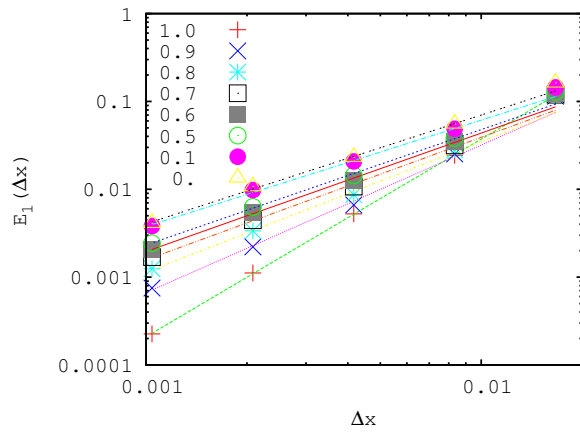
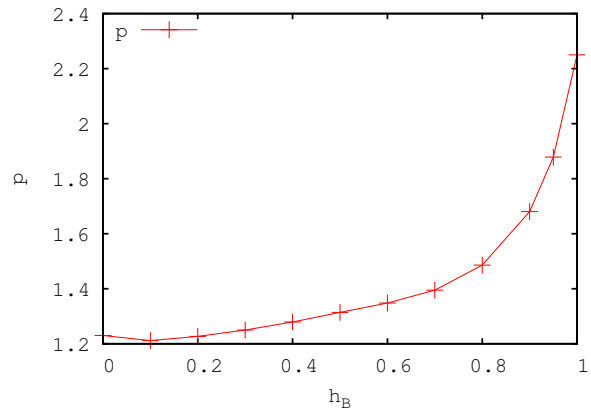


Figure 16: From constant diagonal speed to waterproof interface. Solution at time $t = 0.25$ for three different values of the vertical speed in the SM zone a) $h_B = 0.9$, b) $h_B = 0.5$, c) $h_B = 0.001$

Since the exact solution is not available except for the extreme values, $h_B = 0$ or 1 , we compute the error with a converged solution computed with $\Delta x = 5E - 4$. The different error curves and the variation of the error order with respect to h_B are displayed respectively on panel a) and b) of Figure 17. This numerical experiment confirms that there is a regular drop in precision as the contrast between the vertical speeds on both sides of the interface between zones SM and D increases. It is worth noting that the asymptotic order for the waterproof case ($h_B = 0$) computed using the converged solution is 1.25 instead of the value 1 obtained when using the exact solution in formula (31). On the other hand, the asymptotic order for the reference case with constant diagonal speed ($h_B = 1$) is 2.25, which is less than the asymptotic order 2.4 obtained in the 1D test case 1 for $g_L = g_R = 1$. This small drop in precision is generally encountered with 2D schemes on cartesian grids obtained by tensorization of a 1D scheme.



a) Relative error variation.



b) Order p as function of h_B .

Figure 17: From constant diagonal speed to waterproof interface. a) Relative error and best least-square fit $O(\Delta x^p)$ for different constant h_B values of the vertical speed in zone SM. b) Asymptotic order p as a function of h_B value in zone SM.

Simulation of the biological model

Our latest test performs the convergence study on the full model for the follicular development presented in the paragraph 2.1. However we restrict ourselves to only one follicle $N_f = 1$, and we stop the simulation after a duration $t_N = 1$, short enough so that the computations on very fine grids remain tractable.

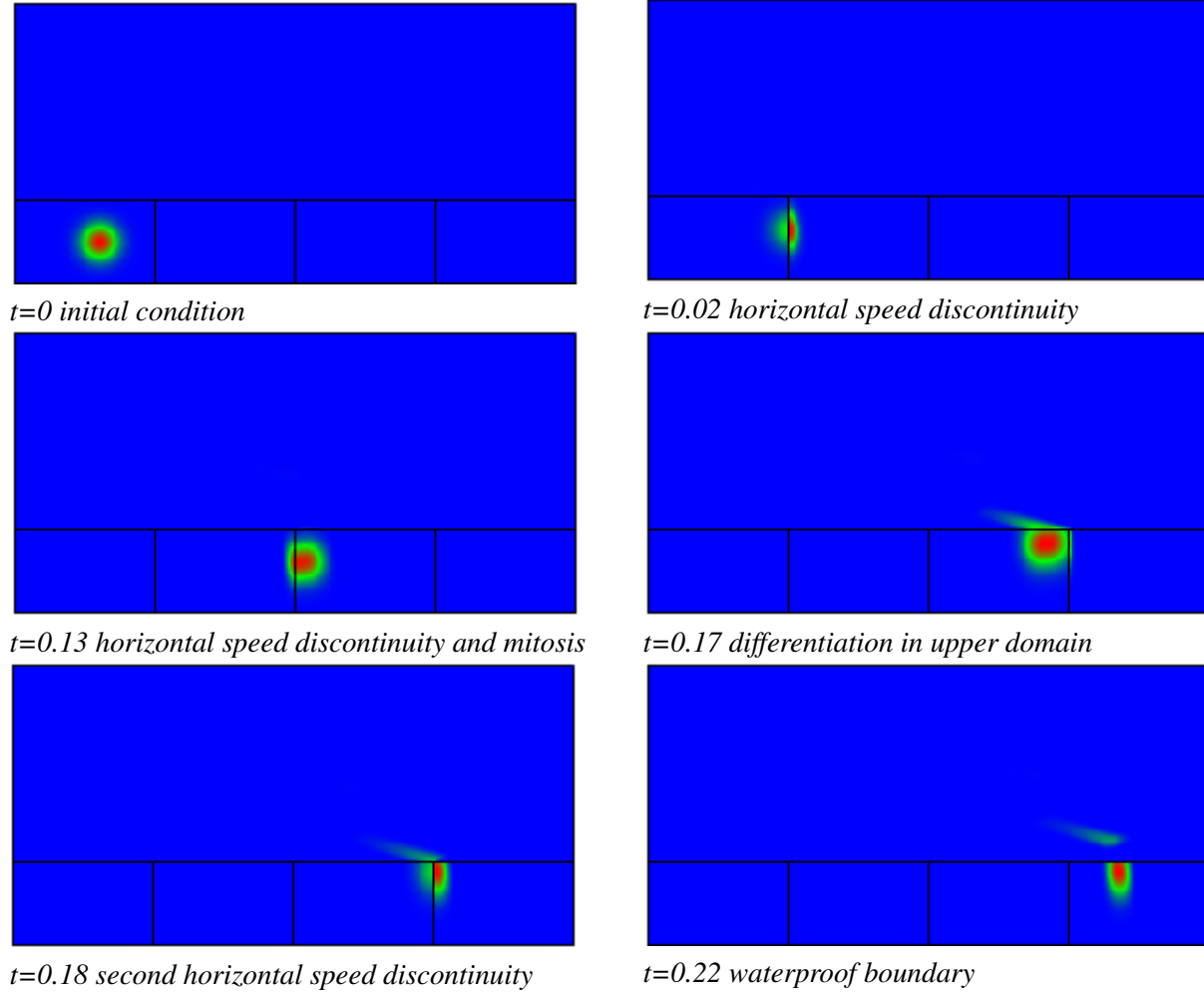


Figure 18: *Third 2D test case : snapshots of the density at different times of the follicular development, $\Delta x = 0.0125$. The color code is time related. Blue and red colors indicate respectively null and maximum density*

The weak non linearity is modeled through the dependance of the speeds and FSH level on the first moment of the density. When dealing with only one follicle, the follicular $m(f, t)$ and ovarian $M(t)$ maturities are equal

$$M(t) = m(1, t) = \int_0^1 \int_0^{N_c D_a} \gamma \phi_1(a, \gamma, t) da d\gamma. \quad (32)$$

The plasma FSH level $U(t)$ showing up in the arguments of the source term in (1) is defined by

$$U(t) = U_{\min} + \frac{1 - U_{\min}}{1 + \exp(c(M(t) - \bar{M}))}, \quad (33)$$

where U_{\min} , c and \bar{M} are real positive constants.

The locally bioavailable FSH level $u_1(t)$ showing up in the arguments of the speeds in (1) is defined by

$$u_1(t) = \min \left(b_1 + \frac{e^{b_2 m(1, t)}}{b_3}, 1 \right) U(t), \quad (34)$$

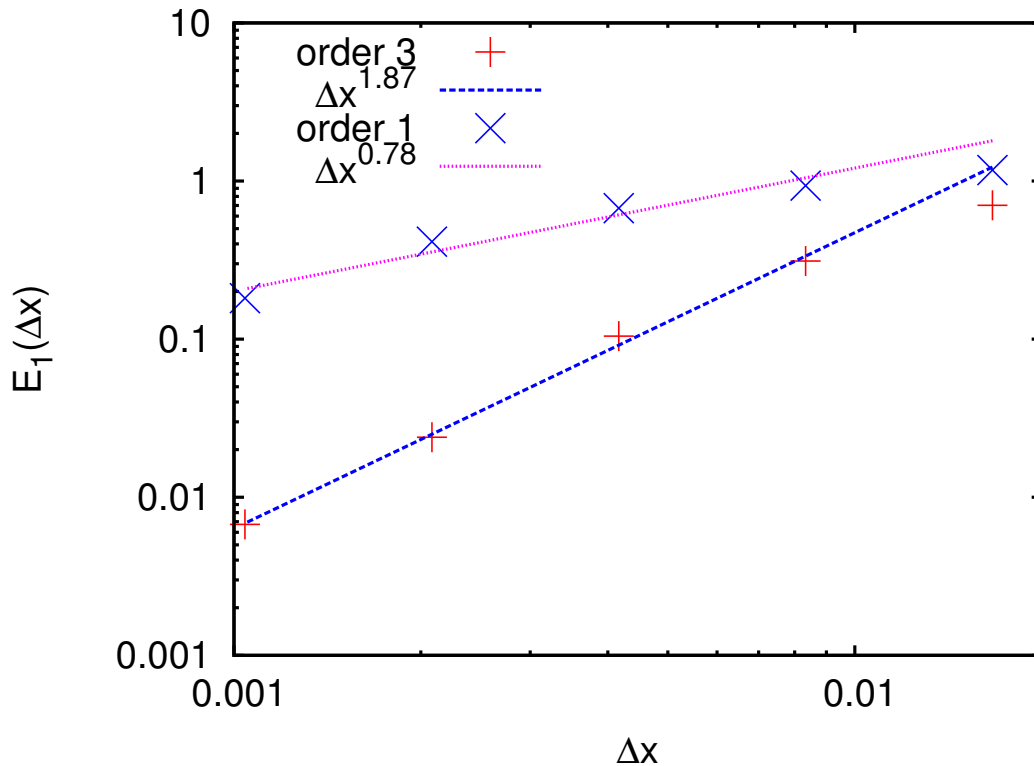


Figure 19: Third 2D test case : follicular development model. Numerical convergence rates with the (order 1 and) order 3 schemes, best least-square fit with $O(\Delta x^2)$.

where b_1 , b_2 and b_3 are real positive constants.

The values of the parameters are gathered in Table 2. The age and maturity speeds parameters have chosen so that, with $t_N = 1$, all of the three interesting transitions : G1-SM, SM-G1 and G1-D do happen, as well as the waterproof phenomenon between zones SM and D. To illustrate these phenomena, snapshots of the density at significant times of the follicular development are displayed on Figure 18. For this simulation, a space discretization $\Delta x = 0.0125$ ($Nm = 80$ cells per half cycle) is used, leading to a varying time discretization of $\Delta t \approx 0.0012$ which meets condition (25) . The numerical convergence of the scheme is illustrated on Figure 19. The relative error with respect to a converged solution obtained using a very fine grid of $Nm = 1920$ cells per half cycle is displayed as a function of the space step Δx . The asymptotic order of convergence computed by least square fitting is almost 2. The biological model combines all the numerical difficulties studied separately in the six previous test cases. As expected, the order of convergence is intermediate between the best and worst order achieved for these toy problems.

References

- [1] M. Adimy, F. Crauste, and S. Ruan. A mathematical study of the hematopoiesis process with applications to chronic myelogenous leukemia. *SIAM Journal on Applied Mathematics*, 65(4):1328–1352, 2005.

Parameter	Description	Value
CFL	CFL condition	0.4
U_{min}	FSH plasma level (eq. (33)) minimum level	0.5
c	slope parameter	2.0
\bar{M}	abscissa of the inflection point	4.5
K	Apoptosis source term (eq. (4)) intensity factor	0.1
$\bar{\gamma}$	scaling factor	0.01
γ_s	cellular maturity threshold	0.3
b_1	intrafollicular FSH level (eq. (34)) basal level	0.08
b_2	exponential rate	2.25
b_3	scaling factor	1450.
g_1	Aging function (eq. (2)) rate	2.
g_2	origin	2.
τ_h	Maturation function (eq. (3))	2.
c_1		0.68
c_2		0.08
\bar{u}		0.02

Table 2: Values of the parameters for the biological model simulation

- [2] A. Ambroso, C. Chalons, F. Coquel, E. Godlewski, F. Lagoutière, P.-A. Raviart, and N. Seguin. Relaxation methods and coupling procedures. *Internat. J. Numer. Methods Fluids*, 56(8):1123–1129, 2008.
- [3] B. Aymard, F. Clément, F. Coquel, and M. Postel. Numerical simulation of the selection process of the ovarian follicles. <http://hal.archives-ouvertes.fr/hal-00656382>, Submitted.
- [4] F. Bouchut and F. James. One-dimensional transport equations with discontinuous coefficients. *Nonlinear Anal.*, 32(7):891–933, 1998.
- [5] B. Boutin, F. Coquel, and LeFloch P. G. Coupling techniques for nonlinear hyperbolic equations. iii. well-balanced approximation of thick interfaces. *arXiv:1205.2437*, 2012.
- [6] R. Bürger and K. H. Karlsen. Conservation laws with discontinuous flux: a short introduction. *J. Engng. Math.*, 60(3-4):241–247, 2008.
- [7] R. Bürger, K. H. Karlsen, and N. H. Risebro. A relaxation scheme for continuous sedimentation in ideal clarifier-thickener units. *Comput. Math. Appl.*, 50(7):993–1009, 2005.
- [8] R. Bürger, K. H. Karlsen, and J. D. Towers. An Engquist-Osher-type scheme for conservation laws with discontinuous flux adapted to flux connections. *SIAM J. Numer. Anal.*, 47(3):1684–1712, 2009.
- [9] N. Echenim, D. Monniaux, M. Sorine, and F. Clément. Multi-scale modeling of the follicle selection process in the ovary. *Math. Biosci.*, 198(1):57–79, 2005.

- [10] E. Godlewski and P.-A. Raviart. The numerical interface coupling of nonlinear hyperbolic systems of conservation laws. I. The scalar case. *Numer. Math.*, 97(1):81–130, 2004.
- [11] S. Gottlieb and C. Shu. Total variation diminishing runge kutta schemes. *Mathematics of computation*, 1998.
- [12] B. Koren. A robust upwind discretisation method for advection, diffusion and source terms. *Numerical Methods for Advection-Diffusion Problems*, 1993.
- [13] B. Perthame. *Transport Equations in Biology*. Birkhäuser Verlag, Basel, 2007.
- [14] N. Seguin and J. Vovelle. Analysis and approximation of a scalar conservation law with a flux function with discontinuous coefficients. *Mathematical Models and Methods in Applied Sciences*, 13(02):221–257, 2003.
- [15] P. Shang. Cauchy problem for multiscale conservation laws : Applications to structured cell populations. <http://arxiv.org/abs/1010.2132>, 2010.
- [16] P. K. Sweby. High resolution schemes using flux limiters for hyperbolic conservation laws. *SIAM J. Numer. Anal.*, 21(5):995–1011, 1984.
- [17] J. J. Tyson and B. Novak. temporal organization of cell cycle. *Current Biology*, 18:R759–768, 2008.

A Exact solutions

We now give the details of the exact solution computations for the 1D and 2D test cases.

A.1 Exact solutions of the 1D problem with piecewise constant speeds

Problem

$$\begin{cases}
 \partial_t \phi + \partial_x g\phi = \Lambda \phi & \text{for } [0, x_s] \cup [x_s, x_L] \\
 g(x) = \begin{cases} g_L & \text{if } x < x_s \\ g_R & \text{if } x \geq x_s \end{cases} & \text{(discontinuous speed)} \\
 \Lambda(x) = \begin{cases} \Lambda_L & \text{if } x < x_s \\ \Lambda_R & \text{if } x \geq x_s \end{cases} & \text{(discontinuous speed)} \\
 \phi(x, 0) = \phi_0(x) & \text{(initial condition)} \\
 \psi_L(g_L \phi(x_s^-, t)) = g_R \phi(x_s^+, t) & \text{(flux condition)}
 \end{cases} \tag{35}$$

Case without source term We first solve this problem when $\Lambda_L = \Lambda_R = 0$, using the method of characteristics. The case when $g_R < g_L$ is displayed in Figure 20. If there were no transmission conditions, the characteristics would be straight lines passing through the vertical axis. The analysis is detailed in the case where g_L and g_R speeds are positive which is the most usual situation in problems arising from biology.

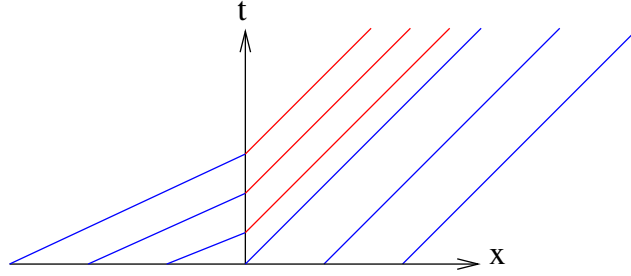


Figure 20: Characteristics of a transmission problem with a transmission condition. The solution is a stationary shock, corresponding to $g_R < g_L \psi'_L$.

Solution For $x < x_s$, considering the characteristics of

$$\begin{cases} \partial_t \phi + g_L \partial_x \phi = 0, \\ \phi(x, 0) = \phi_0(x), \end{cases}$$

the solution is

$$\phi(x, t) = \phi_0(x - g_L t) \quad \text{for } x \leq x_s.$$

Using the same argument, considering the characteristics of

$$\begin{cases} \partial_t \phi + g_R \partial_x \phi = 0, \\ \phi(x, 0) = \phi_0(x), \end{cases}$$

we find that

$$\phi(x, t) = \phi_0(x - g_R t) \quad \text{for } (x - g_R t) \geq x_s.$$

The solution for $(x_0 - g_R t) < (x - g_R t) \leq x_s$ is obtained thanks to the transmission condition

$$\psi_L(g_L \phi(x_s^-, t)) = g_R \phi(x_s^+, t), \quad (36)$$

combined with the fact that

$$\phi(x_s^-, t) = \phi_0(x_s - g_L t),$$

which leads to

$$g_R \phi(x_s^+, t) = \psi_L(g_L \phi(x_s^-, t)) = \psi_L(g_L \phi_0(x_s - g_L t)).$$

Defining a trace function

$$Tr(t) = \frac{1}{g_R} \psi_L(g_L \phi_0(x_s - g_L t)), \quad (37)$$

which acts as a boundary condition, we follow the characteristics

$$\begin{cases} \dot{x}(t) = g_R, \\ x(t_s) = x_s, \end{cases}$$

given by

$$x(t) = x_s + (t - t_s)g_R,$$

to reach x_s , at time

$$t_s = t - \frac{(x - x_s)}{g_R}. \quad (38)$$

Finally, the solution is

$$\phi(x, t) = \begin{cases} \phi_0(x - g_L t) & \text{for } x < x_s, \\ Tr(t_s) & \text{for } (x_s - g_R t) \leq (x - g_R t) < x_s, \\ \phi_0(x - g_R t) & \text{for } (x - g_R t) \geq x_s, \end{cases}$$

where Tr is defined by condition (37) and t_s is defined by (38).

Case with source term It can be deduced from the homogeneous case by changing the unknowns. In the subregion where Λ is constant, if $\phi(x, t)$ is solution of

$$\partial_t \phi + \partial_x g \phi = \Lambda \phi$$

then

$$\tilde{\phi}(x, t) = e^{\Lambda t} \phi(x, t)$$

is solution of

$$\partial_t \tilde{\phi} + \partial_x g \tilde{\phi} = 0.$$

We distinguish two cases :

With a **source term in the left subdomain** $\Lambda_L > 0$ and $\Lambda_R = 0$, the solution is

$$\phi(x, t) = \begin{cases} \phi_0(x - g_L t) \exp(-\Lambda t) & \text{for } x < x_s, \\ Tr(t_s) \exp(-\Lambda t_s) & \text{for } (x_s - g_R t) \leq (x - g_R t) < x_s, \\ \phi_0(x - g_R t) & \text{for } (x - g_R t) \geq x_s. \end{cases}$$

where Tr is defined by the transmission condition (37) and t_s is defined by (38).

With a **source term in the right subdomain** $\Lambda_L = 0$ and $\Lambda_R > 0$, the solution is

$$\phi(x, t) = \begin{cases} \phi_0(x - g_L t) & \text{for } x < x_s, \\ Tr(t_s) \exp(-\Lambda(t - t_s)) & \text{for } (x_s - g_R t) \leq (x - g_R t) < x_s, \\ \phi_0(x - g_R t) \exp(-\Lambda t) & \text{for } (x - g_R t) \geq x_s. \end{cases}$$

where Tr is defined by the transmission condition (37) and t_s is defined by (38).

A.2 Exact solution of the 2D problems with piecewise constant speeds

A.2.1 Horizontal speed

Problem

$$\begin{cases} \partial_t \phi + \partial_x g \phi = 0 & \text{for } (x, y) \in [0, L_x] \times [0, L_y] \\ g(x, y) = \begin{cases} g_L & \text{if } x < x_s \\ g_R & \text{if } x \geq x_s \end{cases} & \text{(discontinuous speed)} \\ \phi(x, y, 0) = \phi_0(x, y) & \text{(initial condition)} \\ \psi_L(\phi(x_s^-, y, t)) = \phi(x_s^+, y, t) & \text{(flux condition)} \end{cases} \quad (39)$$

Solution The solution is

$$\phi(x, y, t) = \begin{cases} \phi_0(x - g_L t, y) & \text{for } x < x_s, \\ Tr(t_s, y) & \text{for } (x_s - g_R t) \leq (x - g_R t) < x_s, \\ \phi_0(x - g_R t, y) & \text{for } (x - g_R t) \geq x_s, \end{cases}$$

where Tr is defined by the transmission condition

$$Tr(t, y) = \psi_L(\phi_0(x_s - g_L t, y)). \quad (40)$$

and t_s is defined by (38).

A.2.2 Shear

Problem

$$\begin{cases} \partial_t \phi + \partial_y \phi = 0 & \text{for } (x, y) \in [0, L_x] \times [0, y_s] \\ \partial_t \phi + \partial_x \phi + \partial_y \phi = 0 & \text{for } (x, y) \in [0, L_x] \times [y_s, L_y] \\ \phi(x, y, 0) = \phi_0(x, y) & \text{(initial condition)} \end{cases} \quad (41)$$

Solution The characteristics are of the form

$$\begin{cases} x(t) = x_0 + t^D \\ y(t) = y_0 + t_s + t^D \end{cases}$$

with t^D the time spent in the upper zone

$$t^D = y - y_s.$$

We can then define the solution piecewise

$$\phi(x, y, t) = \begin{cases} \phi_0(x - t^D, y - t) & \text{for } (x, y) \in [0, L_x] \times [y_s, L_y] \\ \phi_0(x, y - t) & \text{for } (x, y) \in [0, L_x] \times [0, y_s] \end{cases}$$

A.2.3 Waterproof

Problem

$$\begin{cases} \partial_t \phi + \partial_x \phi = 0 & \text{for } (x, y) \in [x_I, L_x] \times [0, y_s] \\ \partial_t \phi + \partial_x \phi + \partial_y \phi = 0 & \text{for } (x, y) \in [0, L_x] \times [0, L_y] - [x_I, L_x] \times [0, y_s] \\ \phi(x, y, 0) = \phi_0(x, y) & \text{(initial condition)} \end{cases} \quad (42)$$

In order to close this problem, we have to add a homogeneous Dirichlet condition on the north of the limit between the 2 zones

$$\phi(x, y_s^+, t) = 0 \quad \text{for } x \in [x_s, L_x]$$

Solution As in the precedent case the characteristics are of the form

$$\begin{cases} x(t) = x_0 + t^D, \\ y(t) = y_0 + t_s + t^D. \end{cases}$$

We can then define the solution piecewise

$$\phi(x, y, t) = \begin{cases} \phi_0(x - t, y - t) & \text{for } (x, y) \in [0, L_x] \times [y_s, L_y] \text{ and } (x - t^D) \leq x_s \\ 0 & \text{for } (x, y) \in [0, L_x] \times [y_s, L_y] \text{ and } (x - t^D) > x_s \\ \phi_0(x - t, y - t) & \text{for } (x, y) \in \mathbf{G1} \\ \phi_0(x - t, y - t_s) & \text{for } (x, y) \in \mathbf{SM} \end{cases}$$